



Atomic sulfur dissimilation remolding ZnIn₂S₄ nanosheets surface to enhance built-internal electric field for photocatalytic CO₂ conversion to syngas

Xingshen Yi, Shuqu Zhang^{*}, Hao Shen, Bing Li, Lixia Yang, Weili Dai, Renjie Song, Jianping Zou, Shenglian Luo

Key Laboratory of Jiangxi Province for Persistent Pollutants Control and Resources Recycle, Nanchang Hangkong University, Nanchang 330063, Jiangxi Province, People's Republic of China

ARTICLE INFO

Keywords:

Se doping
ZnIn₂S₄
Surface remolding
Built-internal electric field
Photocatalytic CO₂ reduction

ABSTRACT

The CO₂ photoreduction of efficiency is severely limited by the sluggish charge kinetics and difficult CO₂ adsorption and activation. In this paper, nonmetallic selenium (Se) doped into ZnIn₂S₄, whose surface were remolded by S atomic dissimilation. Density Functional Theory (DFT) calculated that Se atoms substituted surface sulfur (S) atoms of [In-S] surface layer. The excellent promotion for photoelectric properties of ZnIn₂S₄ with Se dopant benefitted for the adjusted surface properties. The built-internal electric field (B-IEF) was highly enhanced with S atomic dissimilation, which promoted charge separation of interlamination (between the [Zn-S], [S-In-S] and [In-S] layers) and achieved local electron polarization. Finally, ZnIn₂S_{3.5}Se_{0.5} showed the improved adsorption energy and lower activation energy, the performance for CO₂ reduction was 1189.5 μmol·g⁻¹·h⁻¹ for CO and 801.6 μmol·g⁻¹·h⁻¹ for H₂ (CO/H₂: 3:2). This work reveals the relationship between surface/external modification and internal regulation of promoting photocatalytic performance of CO₂ reduction.

1. Introduction

Energy shortage and global warming due to non-renewable fossil fuels overuse are the two major challenges currently to human society [1–3]. Under wide international background of carbon neutrality, photocatalytic CO₂ reduction technology has received a lot of attention by researchers for converting anthropogenic CO₂ into high-value-added fuels directly by using solar energy [4,5]. However, the photocatalytic efficiency of CO₂ conversion is far from the expected target due to tardy carrier migration and high CO₂ activation thermodynamic energy barrier, and it is a long way to arrive industrialized conversion for photocatalytic CO₂ reduction [6].

Generally, the basic reaction processes of photocatalytic CO₂ reduction are as follows: (I) photogenerated carriers generated and separation under light irradiation absorption, (II) carriers migration to photocatalyst surface and electron-hole recombination, (III) CO₂ adsorption and utilization of surface charge, and (IV) CO₂ activation and conversion [7]. The inevitable recombination for photogenerated carriers in photocatalysts leads to their low bulk charge separation

efficiency, which is an important reason for their low photocatalytic efficiency. Besides, the surviving charge still faces the challenges of charge recombination and difficult activation of CO₂ after migrating to the catalyst surface [8]. Therefore, the efficient strategies for surface modification of semiconductor photocatalysts are necessary to facilitate carrier separation and CO₂ adsorption, activation [9–11]. Doping engineering, as one of common methods for surface modification, can effectively enhance the catalytic efficiency of CO₂ reduction reaction [12]. However, the actual role of doping engineering for promoting charge separation is simply discussed usually rather than explored intrinsic mechanism deeply. Zhang et al. reported the greatly improved charge separation efficiency in C-doped Bi₂O₃Cl photocatalyst for the enhanced built-internal electric field (B-IEF) firstly [13]. Since then, the strategy for modulating the B-IEF by heteroatom doping to regulate carrier separation efficiency is gradually coming into the view of researchers [14,15]. The presence of the B-IEF in a layered semiconductor has been reported to be an outstanding strategy to modulate the migration kinetics of charge separation [6,16]. It is well known that the B-IEF of layered materials can be initiated by the non-uniform charge

^{*} Corresponding author.

E-mail address: zhangshuqu2013@126.com (S. Zhang).

<https://doi.org/10.1016/j.apcatb.2023.123003>

Received 7 April 2023; Received in revised form 2 June 2023; Accepted 14 June 2023

Available online 20 June 2023

0926-3373/© 2023 Elsevier B.V. All rights reserved.

distribution between the various component layers for their different chemical compositions [17,18]. Therefore, it is a smart strategy to modulate charge carriers by induced B-IEF for charge unbalance of doping engineering.

In recent years, layered metal sulfide materials with multiple components have been widely used as visible light responsive photocatalytic materials due to their narrow band gap, unique electronic and optical properties. ZnIn_2S_4 , as a typical and layered AB_2X_4 ternary metal sulfide, has researched widely due to its unique layered structure and stability and has attracted many researchers in the field of energy and environment [19–21]. The layered structure of hexagonal ZnIn_2S_4 is composed of alternating stacks of [Zn-S]-[S-In-S]-[In-S] along the z-axis direction [22]. For a half unit cell ZnIn_2S_4 , the surface [In-S] and [Zn-S] layers mainly contribute to the conduction band minimum (CBM) orbital and the valence band maximum (VBM) orbital respectively [23,24]. Under irradiation, photogenerated electrons would transfer from the VBM at the [Zn-S] surface layer to the CBM at the [In-S] surface layer after photoexcitation, arriving the active sites to participate the reduction reaction. The unique asymmetric of layered structure for ZnIn_2S_4 provides practicable prospect to induce B-IEF to modulate the charge dynamics [18]. However, the insufficient driving force of the B-IEF cause lower efficiency of electron-hole separation, which limits its photocatalytic activity and hinder practical photocatalytic application [25, 26]. Xiong and co-workers reported that the B-IEF of ZnIn_2S_4 was enhanced by non-metallic O-doped into [Zn-S] surface layer (VBM), promoting the electron transferring to the CBM at the [In-S] surface layer and resulting in improved photocatalytic performance [27]. Zhou et al. reported that the intrinsic electron potential well of ZnIn_2S_4 was influenced by metal In-doped into [Zn-S] surface layer (VBM), enabling the generated photogenerated electrons to be immediately utilized in the reduction half-reaction [28]. It has not report about modulating B-IEF by tuning the chemical composition of at the [In-S] surface (CBM) for doping engineering of ZnIn_2S_4 . Therefore, it is a promising strategy to construct the doped ZnIn_2S_4 photocatalyst with ordered composition and accurate assemble to modulating B-IEF, which can promote carrier migration and photocatalytic performance.

In this work, nonmetallic selenium (Se) doped ZnIn_2S_4 ($\text{ZnIn}_2\text{S}_{4-x}\text{Se}_x$) nanosheets synthesized by simple hydrothermal method, was applied for photocatalytic CO_2 reduction. The doping site was determined by the incorporation of theoretical calculation and experimental data. The surface properties and photoelectric properties were also discussed synthetically and comprehensively. Se atoms substituting surface sulfur (S) atoms of [In-S] surface layer influence the CBM to modulate B-IEF, promoting carriers separation. Finally, the optimized $\text{ZnIn}_2\text{S}_{4-x}\text{Se}_x$ represented the outstanding activity of photocatalytic CO_2 reduction for syngas conversion. The mechanism of CO_2 adsorption, activation and conversion with enhanced built-internal electric field after surface remodeling was discussed and uncovered in depth.

2. Experimental

2.1. Materials

Zinc chloride (ZnCl_2), indium (III) chloride tetrahydrate ($\text{InCl}_3 \cdot 4\text{H}_2\text{O}$), thioacetamide (TAA), selenium powder, hydrazine hydrate ($\text{N}_2\text{H}_4 \cdot \text{H}_2\text{O}$), polyvinyl pyrrolidone (PVP) were obtained from Sino-pharm Chemical Reagent Co., Ltd. (China). All chemicals were used without further purified in the experiments.

2.2. Synthesis of $\text{ZnIn}_2\text{S}_{4-x}\text{Se}_x$, ZnIn_2S_4 and ZnIn_2Se_4

To synthesize the $\text{ZnIn}_2\text{S}_{4-x}\text{Se}_x$ by a typical hydrothermal method, 1 mmol of ZnCl_2 , 2 mmol of $\text{InCl}_3 \cdot 4\text{H}_2\text{O}$, and 100 mg of PVP were dissolved in 30 mL of deionized water, while 3.9/3.7/3.5/3.3 mmol of TAA and 0.1/0.3/0.5/0.7 mmol of selenium powder were dissolved in 5 mL of $\text{N}_2\text{H}_4 \cdot \text{H}_2\text{O}$ and stir at 80 °C for 5 min. Subsequently, the obtained

reddish-brown solution was added drop to the above deionized aqueous solution and stirred for 30 min. Then, the mixture was retained at 220 °C for 24 h in a 50 mL Teflon-lined autoclave (Anhui Kemi Machinery Technology., LTD, China). After cooling down to room temperature, the precipitates were obtained after ethyl alcohol and deionized water washing for several times. Finally, the $\text{ZnIn}_2\text{S}_{4-x}\text{Se}_x$ ($x = 0.1, 0.3, 0.5, 0.7$) was obtained by drying at 60 °C for 12 h in an oven. The synthesis method of ZnIn_2S_4 was similar to that of $\text{ZnIn}_2\text{S}_{4-x}\text{Se}_x$, except that 4 mmol of TAA added without selenium powder. The synthesis method of ZnIn_2Se_4 was similar to that for $\text{ZnIn}_2\text{S}_{4-x}\text{Se}_x$, except that only 4 mmol of selenium powder added without TAA.

2.3. Characterizations

The surface morphologies and the element mappings of the materials were obtained from a scanning electron microscopy (SEM, ZEISS Sigma 300, Germany). The morphologies and lattice fringes of the materials were obtained from a transmission electron microscopy (TEM, JEOL, JEM-2100 F, Japan) with an accelerating voltage of 200 kV. The crystalline phases composition of all-prepared materials was characterized by a X-ray diffraction (XRD, Bruker D8 Advance, Germany) with Cu K_α ($\lambda = 1.542 \text{ \AA}$). The microstructure of crystalline materials was carried out by Raman spectrum (Raman, Horiba LabRAM HR Evolution, Japan) with 532 nm laser wavelength from 50 ~ 4000 cm^{-1} . The electronic structures and chemical states of elements were analysis by X-ray photoelectron spectroscopy (XPS, Shimadzu KRATOS AXIS SUPRA+, Japan) with an exciting source of Al K_α (0.1 eV). The surface potential of the samples was measured before and after light exposure using a Kelvin probe force microscope (KPFM, Bruker Dimension Icon, Germany). Zeta potential was obtained from Zetasizer Nano (Malvern, ZS90, Britain). Contact angle was carried out to examine the surface hydrophilia of the samples (JY-82 C, Chengde, China). The BET adsorption and desorption isotherms, pore size distribution was performed on a Belsorp-Mini II analyzer (Japan). The surface photovoltage spectra was conducted from a surface photovoltage spectrometer (SPV, CEL-SPS1000, Beijing, China). The second harmonic generation (SHG) signal was tested with an Agilent E5061B network analyzer. The photoluminescence (PL) spectra were obtained and excited at 295 nm by a fluorescence spectrophotometer (Hitachi F4500, Japan) at room temperature. The time-resolved fluorescence spectrofluorometer (TRPL, Edinburgh FS5, Britain) with 295 nm excited wavelength was used to record the fluorescence emission spectra. The photocurrent response was tested in Na_2SO_4 aqueous solution (0.2 M, pH = 6.8) using an electrochemical workstation (Chenhua Instrument Co., Shanghai, China) with a three-electrode electrochemical system that Ag/AgCl electrode, Pt electrode, and fluoride tin oxide (FTO) with covered as-prepared photocatalysts (active area of $1.0 \times 1.0 \text{ cm}^2$) were used as the reference electrode, counter electrode, and working electrode, respectively. The preparation process of the working electrode : 20 mg photocatalysts were dispersed in 200 μL of ethyl alcohol and 30 μL of Nafion to obtain a suspension after ultrasonic treatment, then coated onto the FTO glass substrate uniformly. After that, the coated FTO glass was dried at 60 °C. An integrating sphere-equipped UV-vis spectrophotometer (DRS, Cary 300, America) was used to capture the diffuse reflection spectra (DRS) in the UV-vis range. The intermediate products for CO_2 adsorption and reduction were analyzed from in-situ Fourier transform infrared spectroscopy (in-situ FTIR, Bruker INVENIO R, Germany).

2.4. Photocatalytic CO_2 reduction measurements

The performance evaluation of photocatalytic CO_2 reduction was proceeded in a 50 mL quartz tube at atmospheric pressure and ambient temperature. Typically, 4 mg photocatalyst, 2 μmol CoCl_2 , 15 mg bipyridine, 3 mL acetonitrile, 2 mL H_2O , and 1 mL TEOA were added in a gas-closed quartz tube. The quartz tube was purged with pure CO_2 gas for 30 min to completely remove air and filled with 1.0 atm of pure CO_2 .

A 200 W of white LED lamp ($420\text{ nm} \leq \lambda \leq 800\text{ nm}$) was used as the irradiation source. The temperature was maintained at room temperature and the position of the tube was changed every 30 mins. After the reaction, the generated products (CO and H_2) were analyzed qualitatively and quantitatively by a gas chromatograph (FL GC9790II, Zhejiang, China) equipped with a flame ionization detector (FID) and a thermal conductivity detector (TCD).

3. Results and discussion

3.1. Morphological and structural characterization

The typical preparation process of Se doped ZnIn_2S_4 was presented in Fig. S1. Firstly, TAA and Se powder, as the sources of sulfur and selenium respectively, is dispersed in $\text{N}_2\text{H}_4\text{-H}_2\text{O}$ at 80°C to form a homogeneous red-brown solution, which hold strong reduction properties. Then, above solution is added dropwise to the solution containing polyvinylpyrrolidone (PVP), ZnCl_2 and InCl_3 . The stable microemulsion is formed after mixing of hydrophobic alkyl group of PVP surfactant and $\text{S-N}_2\text{H}_4$ and $\text{Se-N}_2\text{H}_4$. Finally, Se doped ZnIn_2S_4 with ultrathin nanosheet morphology is obtained after Oswald Ripening in the process of hydrothermal method. The microscopic morphologies of ZnIn_2S_4 , $\text{ZnIn}_2\text{S}_{3.5}\text{Se}_{0.5}$ and ZnIn_2Se_4 were characterized using scanning electron microscopy (Fig. 1a-c). It is noteworthy that the morphology of ZnIn_2S_4 transforms from stacking nanosheets to dispersed nanosheets after Se doping, which may facilitate the carrier separation [29]. It is needed to further investigate the effect on the microscopic influences of ZnIn_2S_4 after Se doping.

TEM mapping shows that $\text{ZnIn}_2\text{S}_{3.5}\text{Se}_{0.5}$ displays a uniform

distribution of Zn, In, S, and Se elements (Fig. S2). As depicted in Fig. 1d and Fig. S3a, the lattice spacing of ZnIn_2S_4 is 0.306 nm and 0.330 nm, which are corresponding to the {008} and {101} planes respectively [18,30]. Meanwhile, Fig. 1e and Fig. S3b shows its hexagonal atomic arrangement, revealing a standard hexagonal crystal type ZnIn_2S_4 . The lattice spacings of $\text{ZnIn}_2\text{S}_{3.5}\text{Se}_{0.5}$ are 0.306 nm and 0.353 nm, which are corresponding to the {008} and {007} planes respectively [31]. There is lattice expansion for ZnIn_2S_4 {008} lattice planes after Se doping compared with normal lattice plane (0.325 nm) from Fig. 1f and Fig. S3c). It is attributed that Se atoms substituted S atom cause local lattice distortion (Fig. 1g and Fig. S3d).

XRD spectra was collected to study the phase and crystallographic characteristics of Se doped ZnIn_2S_4 . It confirms the hexagonal structure of ZnIn_2S_4 and $\text{ZnIn}_2\text{S}_{3.5}\text{Se}_{0.5}$ (JCPDS No. 24-1447), which is consistent with the HRTEM analysis (Fig. S4). The characteristic peaks at 22.21° , 25.43° , 26.91° , 27.51° and 47.28° for $\text{ZnIn}_2\text{S}_{3.5}\text{Se}_{0.5}$ are corresponding to {007}, {008}, {101}, {102} and {111} planes, respectively. No other peaks detected indicate that pure $\text{ZnIn}_2\text{S}_{3.5}\text{Se}_{0.5}$ is synthesized successfully. The synthesized pure ZnIn_2Se_4 with 27.01° and 44.82° characteristic peaks (JCPDS No. 39-0458), are corresponding to {112} and {204} planes, respectively. It is worthy to note that all characteristic diffraction peaks of the Se doped ZnIn_2S_4 are shifted to a lower angle compared with ZnIn_2S_4 , especially {007} and {008} lattice peaks (Fig. 1h). It indicates that the lattice is expanded [32]. This transformation can be attributed to the larger ionic radius of Se^{2-} (1.98 \AA) compared with that of S^{2-} (1.84 \AA) [33]. Se atom introduction cause atomic distortion due to surrounding atoms re-arrangement, which is consistent to HRTEM analysis.

Raman spectroscopy is an effective tool to further corroborate the

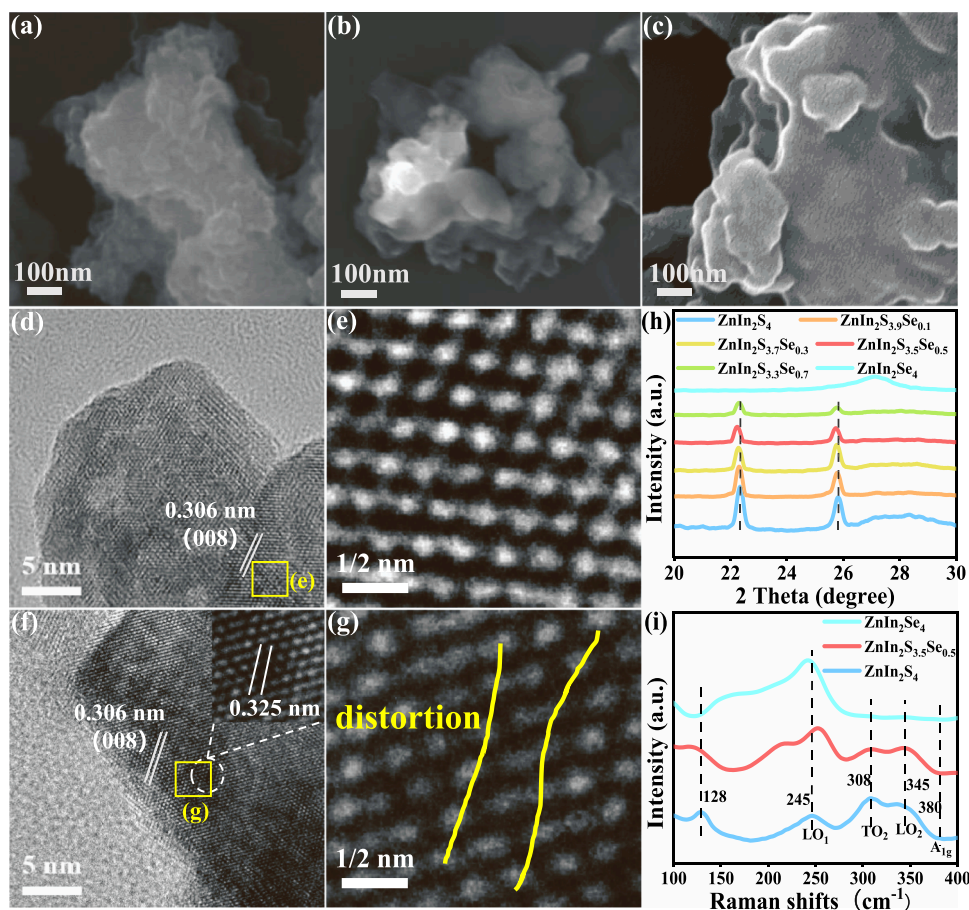


Fig. 1. SEM images of (a) ZnIn_2S_4 , (b) $\text{ZnIn}_2\text{S}_{3.5}\text{Se}_{0.5}$ and (c) ZnIn_2Se_4 . TEM and HRTEM images of (d, e) ZnIn_2S_4 and (f, g) $\text{ZnIn}_2\text{S}_{3.5}\text{Se}_{0.5}$. (h) Partial magnified XRD patterns of ZnIn_2S_4 , $\text{ZnIn}_2\text{S}_{4-x}\text{Se}_x$ ($x = 0.1, 0.3, 0.5, 0.7$) and ZnIn_2Se_4 . (i) Raman spectra of ZnIn_2S_4 , $\text{ZnIn}_2\text{S}_{3.5}\text{Se}_{0.5}$ and ZnIn_2Se_4 .

doping of Se atoms into the ZnIn_2S_4 lattice, as shown in Fig. 1i. Raman spectrum for pure ZnIn_2S_4 shows five characteristic peaks at 128, 245, 308, 345, and 380 cm^{-1} [34,35]. The characteristic peak at 128 cm^{-1} indicates the structural character of layered hexagonal ZnIn_2S_4 . The characteristic peaks at 245 cm^{-1} and 345 cm^{-1} are associated with the longitudinal optical modes (LO_1 and LO_2). The characteristic peak at 308 cm^{-1} and 380 cm^{-1} can be attributed to the transverse optical mode (TO_2) and A_1g mode. $\text{ZnIn}_2\text{S}_{3.5}\text{Se}_{0.5}$ shows reduced intensity and broadening of the characteristic peaks at 128, 308, 345, 380 cm^{-1} compared with ZnIn_2S_4 , which can be attributed to the reduced crystal symmetry due to the influence of Se doping [36,37]. Meanwhile, the increased peak intensity at 245 cm^{-1} of $\text{ZnIn}_2\text{S}_{3.5}\text{Se}_{0.5}$ suggests that Se has been doped into ZnIn_2S_4 successfully. All in all, the Se atoms are introduced into ZnIn_2S_4 lattice with expanded and distorted state.

3.2. Exploration of doping site and doping behavior

X-ray photoelectron spectroscopy (XPS) analysis was carried out to further inspect the chemical states and electronic configuration of elements after Se doping. The full spectrum of ZnIn_2S_4 demonstrates the presence of Zn, In, and S elements, and $\text{ZnIn}_2\text{S}_{3.5}\text{Se}_{0.5}$ reveals the coexistence of Zn, In, S, and Se elements, while ZnIn_2Se_4 with only Zn, In, and Se (Fig. S5a-c). No other peaks of impurities are present as the same as XRD and Raman results, indicating the successful Se doping. Table S1 showed the XPS fitting data of elements area for ZnIn_2S_4 , $\text{ZnIn}_2\text{S}_{3.5}\text{Se}_{0.5}$ and ZnIn_2Se_4 and area ratio of elements. The final compositions are close to the addition ratios of the raw materials. Fig. 2a-d showed High-resolution XPS spectra of Zn 2p, In 3d, S 2p and Se 3d for $\text{ZnIn}_2\text{S}_{3.5}\text{Se}_{0.5}$ and ZnIn_2S_4 . As for Zn 2p, the binding energies of Zn $2p_{1/2}$ and Zn $2p_{3/2}$ are 1044.57 eV and 1021.60 eV for ZnIn_2S_4 , while

1044.60 eV and 1021.63 eV for $\text{ZnIn}_2\text{S}_{3.5}\text{Se}_{0.5}$. The binding energies of Zn 2p for $\text{ZnIn}_2\text{S}_{3.5}\text{Se}_{0.5}$ shift 0.03 eV to higher binding energy compared to that for ZnIn_2S_4 . As for In 3d, 452.12 eV and 444.58 eV are corresponding to the binding energies of In $3d_{3/2}$ and In $3d_{5/2}$ for ZnIn_2S_4 , while 452.02 eV and 444.48 eV for $\text{ZnIn}_2\text{S}_{3.5}\text{Se}_{0.5}$. The binding energies of In 3d for $\text{ZnIn}_2\text{S}_{3.5}\text{Se}_{0.5}$ shift 0.10 eV to lower binding energy compared to that for ZnIn_2S_4 . The S 2p of ZnIn_2S_4 is decomposed into two separated peaks at 162.46 eV and 161.28 eV, which are indexed as S $2p_{1/2}$ and S $2p_{3/2}$, respectively, while 162.70 eV and 161.52 eV for $\text{ZnIn}_2\text{S}_{3.5}\text{Se}_{0.5}$. As for Se 3d, $\text{ZnIn}_2\text{S}_{3.5}\text{Se}_{0.5}$ has two peaks at 54.83 eV (Se $3d_{3/2}$) and 53.97 eV (Se $3d_{5/2}$), while ZnIn_2S_4 has no Se 3d peaks. The binding energies of S 2p for $\text{ZnIn}_2\text{S}_{3.5}\text{Se}_{0.5}$ shift 0.24 eV to higher binding energy compared to that for ZnIn_2S_4 . Compared with the shift level of Zn 2p and In 3d, Se atom may substitute S atom adjacent with In atom [27,38]. The negative shift of In 3d and positive shift of S 2p after Se doping in ZnIn_2S_4 indicate that surface charges are accumulated near In atom adjacent with Se atom. It is due to the weaker electronegativity (Se and S: 2.40 and 2.50) and the lower electron gaining ability of Se than S.

Density Functional Theory (DFT) calculation were conducted to further clarify Se doping sites and behavior mechanism arising from Se doping. The calculation methods were described in the calculation details (Text S1). The layered structure of hexagonal ZnIn_2S_4 is composed of alternating stacks of [Zn-S]-[S-In-S]-[In-S] along the z-axis direction (Fig. S6). There are four structural models of Se substitution in ZnIn_2S_4 : S atoms of [Zn-S] layer, S atoms of [Zn-S-In] layer, S atoms of [In-S-In] layer and S atoms of [In-S] layer (Fig. 2e-h). The Se doping site can be determined by the compared substituting energy of S (E_s). The E_s is calculated to be 0.649, 0.564, 0.603, 0.536 eV respectively. It is obvious that Se substituting the surface S atom of [In-S] layer needs the lowest

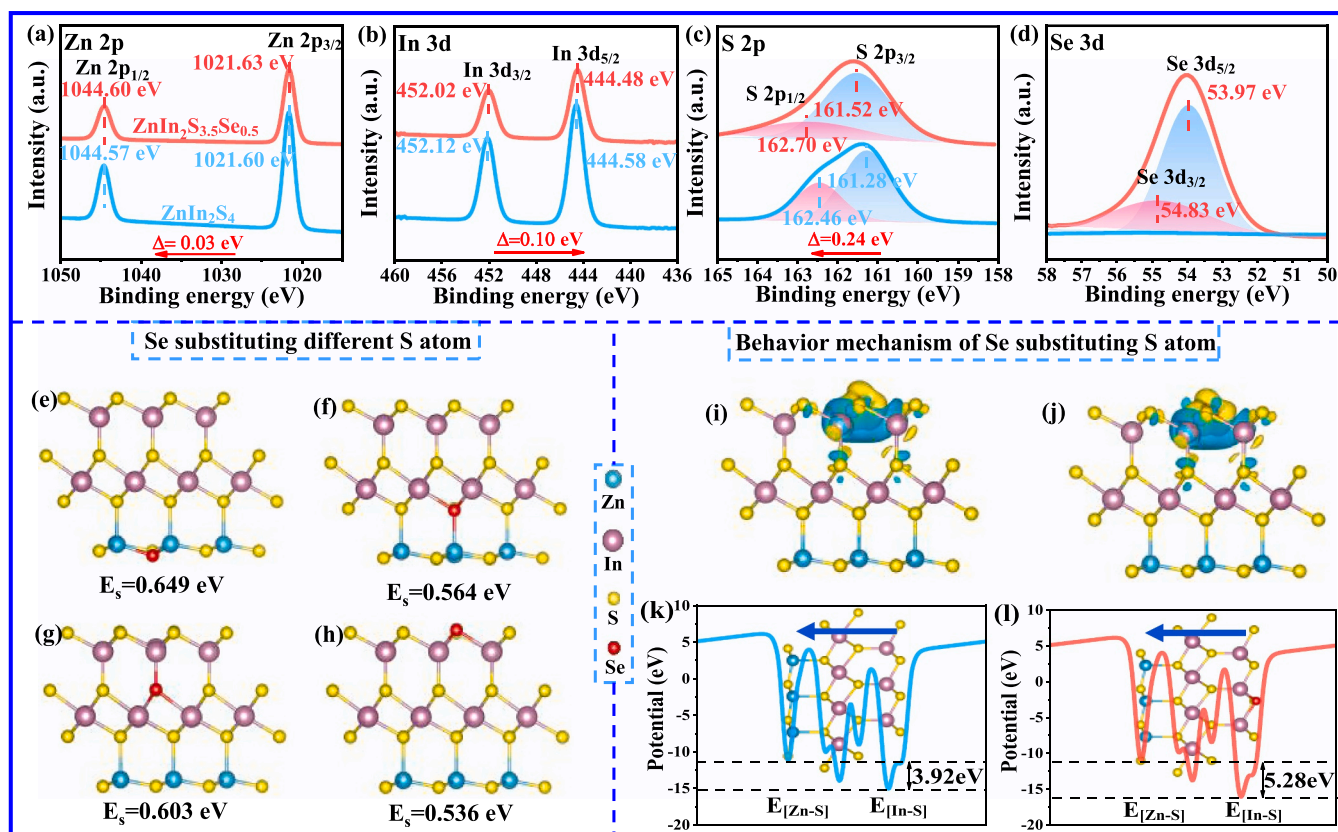


Fig. 2. High-resolution XPS spectra of (a) Zn 2p, (b) In 3d, (c) S 2p and (d) Se 3d for ZnIn_2S_4 and $\text{ZnIn}_2\text{S}_{3.5}\text{Se}_{0.5}$. Structural model and substituting energy (E_s) for atomic Se substituting different S atoms in ZnIn_2S_4 : (e) S atoms of [Zn-S] layer, (f) S atoms of [Zn-S-In] layer, (g) S atoms of [In-S-In] layer and (h) S atoms of [In-S] layer and corresponding E_s . Differential charge density of (i) ZnIn_2S_4 and (j) $\text{ZnIn}_2\text{S}_{3.5}\text{Se}_{0.5}$. (The yellow color represents charge accumulation and the blue color represents charge depletion) Electrostatic potentials for (k) ZnIn_2S_4 and (l) $\text{ZnIn}_2\text{S}_{3.5}\text{Se}_{0.5}$.

substitution energy ($E_s=0.536$ eV). Se doped into ZnIn_2S_4 tends to substitute the S of [In-S] layer certainly combining XPS analysis and calculation results. Differential charge density and electrostatic potentials were calculated to further investigate the electronic behavior and B-IEF after Se doping. As the same as XPS analysis, Se doping promotes surface charges to accumulate the areas In atom adjacent with Se atom, resulting in local charge polarization of ZnIn_2S_4 [In-S] layer (Fig. 2i and j). Se atom substituting S atom of [In-S] layers break the atomic homogenization of ZnIn_2S_4 surface, which cause the inhomogeneous charge distribution and more negative potential for [In-S] layer. Fig. 2k showed the calculated electrostatic potential of the ZnIn_2S_4 . Notably, unequal charge distribution and electrostatic potential between the [Zn-S], [S-In-S] and [In-S] layers suggest the presence of vertical B-IEF within pure ZnIn_2S_4 , which drive the internal separation of charge carriers. The direction of B-IEF is opposite to the electron transfer direction, pointing from the [In-S] layer to the [Zn-S] layer. The B-IEF intensity within pure ZnIn_2S_4 is estimated by the difference value in local electrostatic potential (ΔE) between the [Zn-S] and [In-S] layers for quantitative analysis. $\text{ZnIn}_2\text{S}_{3.5}\text{Se}_{0.5}$ exhibits a larger ΔE (5.28 eV) compared to that of pure ZnIn_2S_4 (3.92 eV), indicating the stronger B-IEF within it (Fig. 2l). Such an enhanced B-IEF effectively promotes photogenerated carrier separation and suppresses bulk electron-hole pair complexation. The above theoretical calculations indicate the directivity and the enhanced intensity of B-IEF.

The B-IEF magnitude could be calculated according to the Kanata's model, which is related to surface charge density, Zeta potential and surface potential [13]. It is reported that the Kanata's model as following Eq. (1) [39–43] :

$$E = (-2V_s\rho/\epsilon\epsilon_0)^{1/2} \quad (1)$$

Where E is B-IEF value, V_s is the surface voltage, ρ is the surface charge density, ϵ is the low-frequency dielectric constant, and ϵ_0 is the vacuum dielectric constant. ϵ and ϵ_0 are two constants, so B-IEF is mainly determined by the surface potential and the surface charge density. The V_s can be obtained from AFM with KPFM model (Fig. 3a and b). The corresponding potential difference (ΔCPD) before and after light exposure is 7.23 mV and 11.20 mV for ZnIn_2S_4 and $\text{ZnIn}_2\text{S}_{3.5}\text{Se}_{0.5}$, respectively. The ρ can be tested and calculated by the according to the following Eq. (2):

$$\rho = \sqrt{8kT\epsilon\epsilon_0 n \sinh(z e_0 \phi_0 / 2kT)} \quad (2)$$

Where k is the Boltzmann constant, T is absolute temperature, n is Number of electrolytes per unit volume, e_0 is electron charge, z is electrolyte valence, ϕ_0 is surface potential. For the ϕ_0 , there is an approximately Eq. (3):

$$\phi_0 = \xi(1 + D/\alpha_1)e^{\kappa D} \quad (3)$$

ξ is Zeta potential (23.30 for ZnIn_2S_4), 27.50 for $\text{ZnIn}_2\text{S}_{3.5}\text{Se}_{0.5}$), which can be obtained by experimental examine (Fig. 3c), D is distance from Sliding Layer to Particle Surface, α_1 is Particle Stokes radius, κ is Debye length. From the above equations, the B-IEF (E) can be approximately concluded into a function of surface potential V_s and Zeta potential ξ :

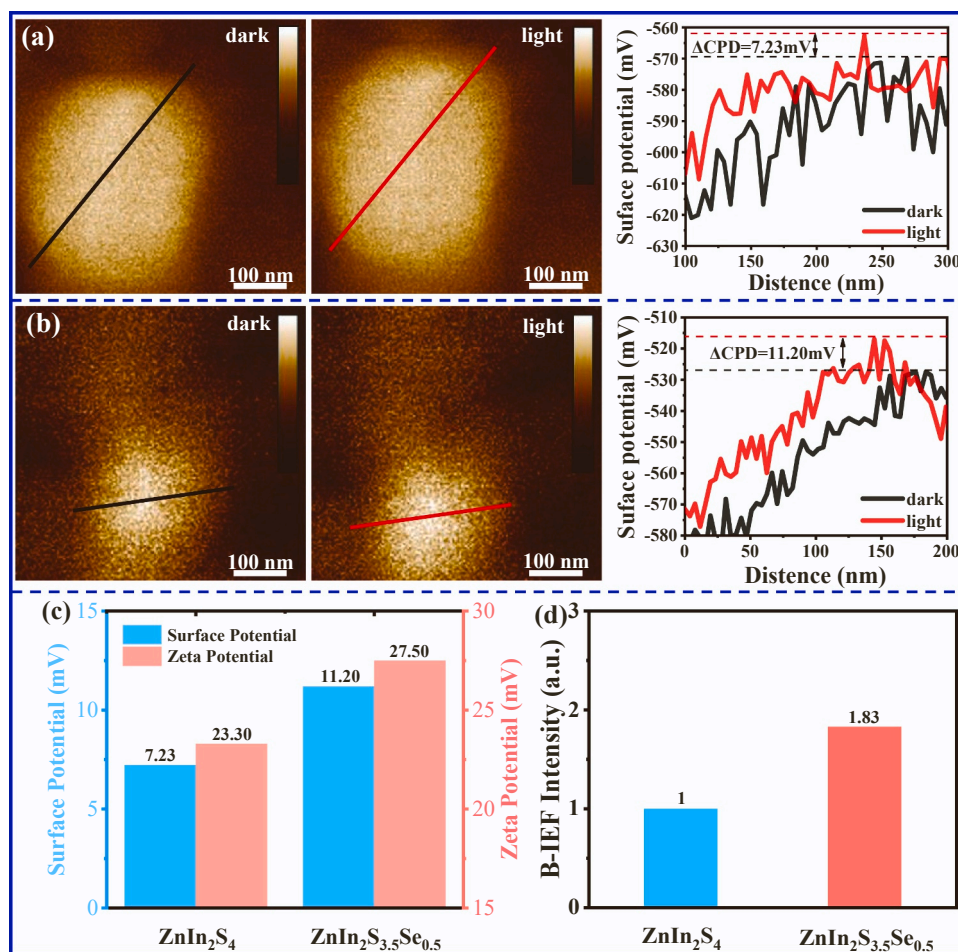


Fig. 3. KPFM potential images of (a) ZnIn_2S_4 and (b) $\text{ZnIn}_2\text{S}_{3.5}\text{Se}_{0.5}$ in dark and light, and the corresponding potential different (ΔCPD) curves along straight line of the image. (c) Surface potential, Zeta potential and (d) B-IEF intensity of ZnIn_2S_4 and $\text{ZnIn}_2\text{S}_{3.5}\text{Se}_{0.5}$.

$$E = (AV_S \sinh(\frac{ze_0 \xi (1 + D/\alpha_1) e^{kD}}{2kT}))^{1/2} \quad (4)$$

It can be clearly seen from Eq. (4) (A is simplified constant), the B-IEF will increase with the increase of V_S and ξ . Then the B-IEF intensity of ZnIn_2S_4 is normalized as “1”, and as such, the B-IEF intensity of $\text{ZnIn}_2\text{S}_{3.5}\text{Se}_{0.5}$ is obtained to be 1.83 (Fig. 3d). The increased surface potential from experimental data and B-IEF magnitude from Kanata’s model prove that surface modification of Se doping could modulate internal properties of B-IEF efficiently for promoting electrons migration. All in all, Se atoms substituting S atoms of [In-S] layer accelerate surface charges to accumulate the areas In atom adjacent with Se atom, and cause the stronger B-IEF to suppresses bulk recombination and promote separation for photogenerated carriers.

3.3. Characterization of surface and photoelectric properties, bandgap structure

DFT calculation indicated that surface remodeling of atomic dissimulation (Se atom substituting S atom of [In-S] layers) could regulate internal properties (promoting B-IEF intensity) of photocatalyst. It is needed to investigate surface and photoelectric properties generally in experimentally. The static contact angles of different photocatalysts were measured to investigate surface hydrophilicity (Fig. S7). The static

contact angle for ZnIn_2S_4 , $\text{ZnIn}_2\text{S}_{4-x}\text{Se}_x$ ($x = 0.1, 0.3, 0.5, 0.7$) and ZnIn_2Se_4 is 68.09° , 62.37° , 58.11° , 54.16° , 66.87° and 68.30° respectively (Fig. 4a). The contact angle of $\text{ZnIn}_2\text{S}_{3.5}\text{Se}_{0.5}$ is smallest among all the examined photocatalysts. It is reported that the surface hydrophilicity can improve photocatalytic performance of CO_2 reduction [23]. The specific surface areas of ZnIn_2S_4 , $\text{ZnIn}_2\text{S}_{4-x}\text{Se}_x$ ($x = 0.1, 0.3, 0.5, 0.7$) and ZnIn_2Se_4 (shown in Fig. S8) were 14.9, 28.4, 30.0, 31.9, 19.2 and 14.7 , respectively, with $\text{ZnIn}_2\text{S}_{3.5}\text{Se}_{0.5}$ holding the largest specific surface area. The larger average pore size of $\text{ZnIn}_2\text{S}_{3.5}\text{Se}_{0.5}$ compared to ZnIn_2S_4 is also beneficial for CO_2 adsorption (Fig. 4b). Surface photovoltage (SPV) spectra is an important means for monitoring the charge separation, transferring and accumulation in Fig. 4c. ZnIn_2S_4 , $\text{ZnIn}_2\text{S}_{3.5}\text{Se}_{0.5}$ and ZnIn_2Se_4 exhibited distinct SPV responses in the range of $300 \sim 550$ nm [44,45]. The main SPV peaks of ZnIn_2S_4 and $\text{ZnIn}_2\text{S}_{3.5}\text{Se}_{0.5}$ is around 350 nm, while ZnIn_2Se_4 exhibited a broader peak. Meanwhile, the positive signal of ZnIn_2S_4 , $\text{ZnIn}_2\text{S}_{3.5}\text{Se}_{0.5}$ and ZnIn_2Se_4 indicates efficient separation in the bulk and ordered migration to the surface for photogenerated carriers, which present behavior of n-type semiconductors [46]. The enhanced surface photovoltage of $\text{ZnIn}_2\text{S}_{3.5}\text{Se}_{0.5}$ indicates the richer density of accumulated photo-generated electrons on $\text{ZnIn}_2\text{S}_{3.5}\text{Se}_{0.5}$. The charge density contour plots of ZnIn_2S_4 and $\text{ZnIn}_2\text{S}_{3.5}\text{Se}_{0.5}$ was also supplemented to inspect electron localization (Fig. 4d-g). It shows that Se atoms substituting S atom breaks the atomic S homogenization on [In-S] layer of ZnIn_2S_4 , leading

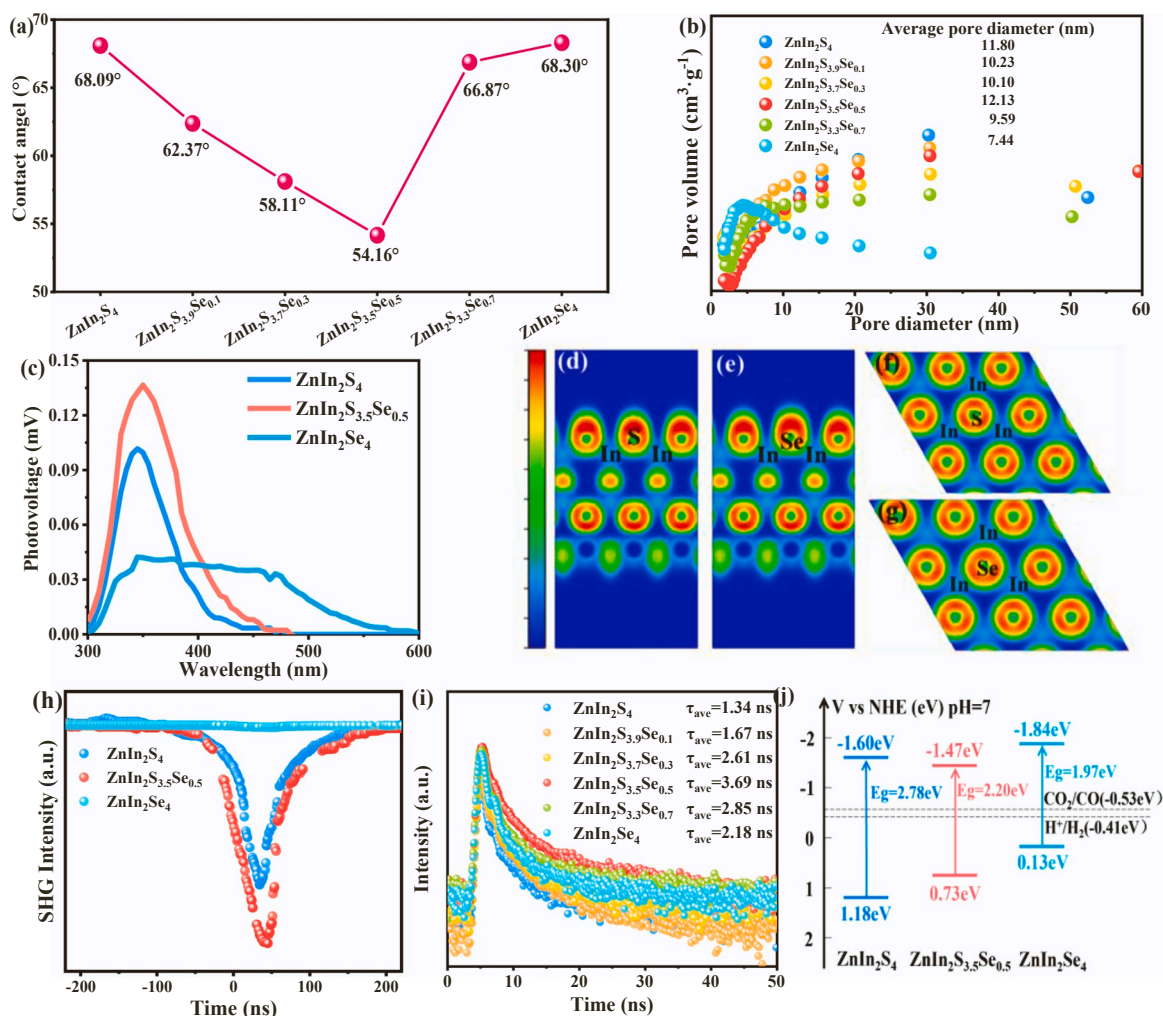


Fig. 4. (a) Static contact angle and (b) the pore size distribution curves of ZnIn_2S_4 , $\text{ZnIn}_2\text{S}_{4-x}\text{Se}_x$ ($x = 0.1, 0.3, 0.5, 0.7$) and ZnIn_2Se_4 . (c) SPV spectrum for ZnIn_2S_4 , $\text{ZnIn}_2\text{S}_{3.5}\text{Se}_{0.5}$ and ZnIn_2Se_4 . The charge density contour plots of (d) side view and (f) top view for ZnIn_2S_4 , (e) side view and (g) top view for $\text{ZnIn}_2\text{S}_{3.5}\text{Se}_{0.5}$. (h) SHG signals for ZnIn_2S_4 , $\text{ZnIn}_2\text{S}_{3.5}\text{Se}_{0.5}$ and ZnIn_2Se_4 . (i) TRPL decay spectra of ZnIn_2S_4 , $\text{ZnIn}_2\text{S}_{4-x}\text{Se}_x$ ($x = 0.1, 0.3, 0.5, 0.7$) and ZnIn_2Se_4 and (j) Band structures of ZnIn_2S_4 , $\text{ZnIn}_2\text{S}_{3.5}\text{Se}_{0.5}$ and ZnIn_2Se_4 .

to in-homogenous charge distribution. Meanwhile, the electron-gaining ability for Se is poorer than that for S due to the weaker electronegativity of Se (Se: 2.4, S: 2.5). The electrons are tended to accumulate on adjacent In atom with Se. Besides, second harmonic generation (SHG) further reveals the macroscopic polarity difference between ZnIn_2S_4 and $\text{ZnIn}_2\text{S}_{3.5}\text{Se}_{0.5}$ (Fig. 4h) [47]. Obviously, $\text{ZnIn}_2\text{S}_{3.5}\text{Se}_{0.5}$ produces the largest SHG reaction, which means that the $\text{ZnIn}_2\text{S}_{3.5}\text{Se}_{0.5}$ surface is more polarized than the ZnIn_2S_4 and ZnIn_2Se_4 surfaces. Likewise, the enhanced B-IEF also actuate photogenerated electrons to the surface from the higher photocurrent density of Se doped ZnIn_2S_4 samples in Fig. S9a. The photoluminescence (PL) spectra was examined to investigated the separation behavior of photogenerated carriers in Fig. S9b. Se doped ZnIn_2S_4 showed the reduced luminescence intensity compared to pure ZnIn_2S_4 , and the lowest intensity for $\text{ZnIn}_2\text{S}_{3.5}\text{Se}_{0.5}$, indicating that Se dopants in ZnIn_2S_4 can promote carriers separation under powerful driving force of enhanced B-IEF. Besides, time-resolved photoluminescence (TRPL) experiments were performed to study the lifetimes of photogenerated carriers in Fig. 4i. The average electron lifetimes of the photocatalysts are 1.34, 1.67, 2.61, 3.69, 2.85 and 2.18 ns, respectively. The $\text{ZnIn}_2\text{S}_{3.5}\text{Se}_{0.5}$ holds the longest electron lifetime, which is about 2.75 times for pure ZnIn_2S_4 , indicating the suppressed charge recombination under enhanced B-IEF to participate in the CO_2 reduction efficiently.

The bandgap structure should be explored seriously beside of surface and photoelectric properties. Density of states (DOS) profiles (Fig. S10) shows that Se dopants substituting S atoms presents substantial increase in VBM and CBM density, which indicates enhanced capacities of electron donating and electron accepting and increased carrier concentration [18]. Moreover, the bandgap is narrowed and new energy levels appear at the bottom of the CB, which are contributed by In, S and Se. Se atoms doping affects the distribution of In and S atoms in the lattice, resulting in orbital hybridization between In, S and Se atoms [48]. In short, Se doping shortens the bandgap and enhances the carrier concentration, which promotes optical absorption and charge separation. As depicted in UV-vis diffuse reflectance spectroscopy (DRS) (Fig. S11a), pure ZnIn_2S_4 shows an absorption edge at about 550 nm, while the intrinsic absorption edge of Se doped ZnIn_2S_4 samples shows significant red shift with increasing Se doping. The color of the photocatalyst samples change from a visual yellowish to an orange-red (Fig. S12a-f). The band gaps of ZnIn_2S_4 , $\text{ZnIn}_2\text{S}_{3.5}\text{Se}_{0.5}$, and ZnIn_2Se_4 samples is calculated to be 2.78, 2.20, and 1.97 eV, respectively, by the Kubelka-Munk function (Fig. S11b). Meanwhile, valence band levels of ZnIn_2S_4 , $\text{ZnIn}_2\text{S}_{3.5}\text{Se}_{0.5}$, and ZnIn_2Se_4 samples is estimated to be 1.18, 0.73, and 0.13 eV respectively from XPS valence band (VB) spectroscopy (Fig. S11c). The conduction band (CB) levels are calculated to be -1.60, -1.47, and -1.84 eV, respectively. Eventually, the diagram of band structure was shown in Fig. 4j. As can be seen, all prepared photocatalysts fulfill potential requirement for CO_2 conversion to CO absolutely from the bandgap structure. The Se doped ZnIn_2S_4 photocatalyst will present efficient photocatalytic activity for CO_2 reduction, which is benefitted for better surface properties, enhanced photoelectric properties, suitable bandgap structure.

3.4. Photocatalytic performance for CO_2 conversion

The photocatalytic performance of CO_2 reduction was performed in a system with white LED lamp as the light source, H_2O and acetonitrile as the solution, and $\text{Co}(\text{bpy})_3^{2+}$ ($\text{bpy} = 2, 2'$ -bipyridine) and triethanolamine (TEOA) as the co-catalyst and sacrificial agent, respectively. The product chromatograms (CO and H_2) for the CO_2 reduction over ZnIn_2S_4 , $\text{ZnIn}_2\text{S}_{4-x}\text{Se}_x$ ($x = 0.1, 0.3, 0.5, 0.7$) and ZnIn_2Se_4 photocatalysts with retention time at 5.3 min and 2.3 min were shown in Fig. S13. It is clearly that the photocatalytic CO_2 reduction products are indeed CO and H_2 combined with the gas chromatographic peak times (about 5.3 min and 2.3 min) for the CO and H_2 standards (Fig. S14a and Fig. S15a). Subsequently, the yields of photocatalytic CO_2 reduction can

be calculated from the standard curves of CO and H_2 (Fig. S14b and Fig. S15b). The photocatalytic performance of pure ZnIn_2S_4 is $307.5 \mu\text{mol}\cdot\text{g}^{-1}\cdot\text{h}^{-1}$ for CO and $609.2 \mu\text{mol}\cdot\text{g}^{-1}\cdot\text{h}^{-1}$ for H_2 (CO/ H_2 molar ratio is 1:2) in Fig. 5a. The photocatalytic performance for CO_2 conversion over $\text{ZnIn}_2\text{S}_{4-x}\text{Se}_x$ samples ($x = 0.1, 0.3, 0.5, 0.7$) increases with Se incorporation. The $\text{ZnIn}_2\text{S}_{3.5}\text{Se}_{0.5}$ shows the most excellent performance for CO_2 conversion rate (CO: $1189.5 \mu\text{mol}\cdot\text{g}^{-1}\cdot\text{h}^{-1}$ and H_2 : $801.6 \mu\text{mol}\cdot\text{g}^{-1}\cdot\text{h}^{-1}$, CO/ H_2 molar ratio is 3/2), which is about 3.87 and 1.32 times than for pure ZnIn_2S_4 . It also shows good photocatalytic performance compared with other reported ZnIn_2S_4 -based photocatalyst systems for photocatalytic CO_2 reduction (Table S2). It is noticed that the performance decrease when the amount of Se substitution continued to increase. With the increasing Se amount, the XRD peak intensity of $\text{ZnIn}_2\text{S}_{3.7}\text{Se}_{0.3}$ is reduced and the characteristic peak at 27.01° (JCPDS No. 39-0458) is enhanced compared to $\text{ZnIn}_2\text{S}_{3.5}\text{Se}_{0.5}$, indicating a second phase formation in ZnIn_2Se_4 (Fig. S16). The new second phase may act as recombination center of photogenerated charge, thus leading to performance degradation for CO_2 reduction. Moreover, both ZnIn_2S_4 and $\text{ZnIn}_2\text{S}_{3.5}\text{Se}_{0.5}$ exhibits durable photocatalytic reactivity for 4 h photoreaction, producing CO of $1230 \mu\text{mol}\cdot\text{g}^{-1}$ and $4387.5 \mu\text{mol}\cdot\text{g}^{-1}$, and H_2 of $2437.5 \mu\text{mol}\cdot\text{g}^{-1}$ and $2785 \mu\text{mol}\cdot\text{g}^{-1}$, respectively (Fig. 5b). The assessment for photocatalytic performance of CO_2 reduction indicates that Se atom substituting S atom of [In-S] layers improve the photocatalytic efficiency of CO_2 reduction significantly. A series of controlled experiments were conducted to investigate the effect of experimental conditions (Fig. 5c). The results suggest that the catalyst, illumination, CO_2 , co-catalyst ($\text{Co}(\text{bpy})_3^{2+}$) and sacrificial agent (TEOA) are necessary for the photocatalytic CO_2 reduction reaction. Meanwhile, there are $400.8 \mu\text{mol}\cdot\text{g}^{-1}\cdot\text{h}^{-1}$ for H_2 evolution and no CO production in the photocatalytic CO_2 reduction, which indicate that the generated CO are originated from CO_2 conversion. Wavelength-dependent photocatalytic performance of CO_2 reduction over ZnIn_2S_4 and $\text{ZnIn}_2\text{S}_{3.5}\text{Se}_{0.5}$ was inspected in Fig. S17. As discerned, the CO and H_2 yield over ZnIn_2S_4 and $\text{ZnIn}_2\text{S}_{3.5}\text{Se}_{0.5}$ matched well with the UV-vis absorption spectrum, confirming that the CO_2 reduction reaction was certainly triggered by irradiation. Detailly, the CO (H_2) yield over ZnIn_2S_4 and $\text{ZnIn}_2\text{S}_{3.5}\text{Se}_{0.5}$ is 287.1 (638.2) and 1112.1 (941.5), 215.6 (488.2) and 839.8 (690.7), 114.8 (282.4) and 546.4 (503.6), 22.3 (51.2) and 154.4 (165.8), 1.3 (11.7) and 4.9 (22.2) $\mu\text{mol}\cdot\text{g}^{-1}\cdot\text{h}^{-1}$ under 350, 420, 450, 500, 550 nm respectively. Finally, the photocatalytic activity of CO_2 reduction over $\text{ZnIn}_2\text{S}_{3.5}\text{Se}_{0.5}$ maintains stable after five cycles examination (Fig. 5d). XRD pattern, morphology characteristics (SEM image and TEM image) of $\text{ZnIn}_2\text{S}_{3.5}\text{Se}_{0.5}$ after 5 cyclic reaction for photocatalytic CO_2 reduction were investigated (Fig. S18). There is no significant change in crystal structure or surface morphology after five recycle experiments, which indicates the outstanding durability of $\text{ZnIn}_2\text{S}_{3.5}\text{Se}_{0.5}$.

3.5. Mechanism discussion for CO_2 conversion

The intermediates in the process of CO_2 adsorption, activation and conversion on the surface of $\text{ZnIn}_2\text{S}_{3.5}\text{Se}_{0.5}$ were precisely tracked by in situ FTIR spectra to gain insight into the reaction pathway and mechanism for CO_2 reduction. As shown in Fig. 6a, the new peaks appeared and gradually increased at 1283, 1310, 1361, 1420, 1486, 1693 and 2076 cm^{-1} with increasing irradiation time. Among them, the peaks at 1310 and 1361 cm^{-1} are attributed to the $\nu_s(\text{CO}_3)$ mode of bidentate carbonate species ($^*\text{b-CO}_3^{2-}$), and the peak around 1486 cm^{-1} is assigned to the $\nu_s(\text{CO}_3)$ mode of monodentate carbonate species ($^*\text{m-CO}_3^{2-}$) [49, 50]. The peak areas of $^*\text{b-CO}_3^{2-}$ are much larger than that of $^*\text{m-CO}_3^{2-}$, which indicates that double bond is the main intermediates form in the process of adsorption and activation of CO_2 molecule over $\text{ZnIn}_2\text{S}_{3.5}\text{Se}_{0.5}$ [51,52]. Meanwhile, the gradual increasing of 1283, 1420 and 1693 cm^{-1} peaks indicate the formation and accumulation of $^*\text{COOH}$ on $\text{ZnIn}_2\text{S}_{3.5}\text{Se}_{0.5}$, which are attributed to the O-H bending, C-O stretching and C=O stretching respectively [53–55]. And the peak at 2076 cm^{-1}

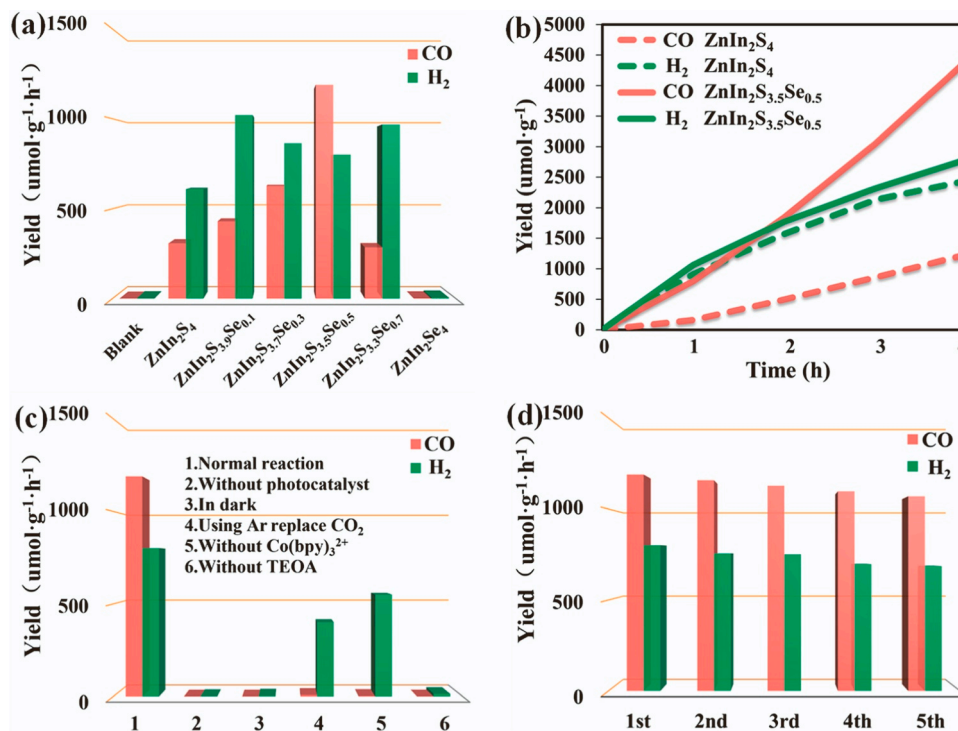


Fig. 5. (a) Visible-light-driven CO₂ reduction of Blank, ZnIn₂S₄, ZnIn₂S_{4-x}Se_x ($x = 0.1, 0.3, 0.5, 0.7$) and ZnIn₂Se₄. (b) Time-yield plots of CO and H₂ over ZnIn₂S₄ and ZnIn₂S_{3.5}Se_{0.5}. (c) Photocatalytic CO₂ reduction performance under various reaction conditions and (d) cyclic stability test of ZnIn₂S_{3.5}Se_{0.5}.

indicates the generation of CO as a final product. Besides, peaks at 2374, 2348, and 2317 cm⁻¹ are attributed to asymmetric stretching of surface CO₂ molecules (Fig. S19a). At the same time, adsorbed gas-phase CO₂ are also detected at 3725, 3705, 3625, and 3592 cm⁻¹, accompanied by surface-bound OH⁻ separated from adsorbed H₂O (~3538 cm⁻¹) from weak overtone bands (Fig. S19b) [56]. Based on the above analysis, a possible mechanism for the CO₂ reduction half-reaction occurring on the surface of ZnIn₂S_{3.5}Se_{0.5} is deduced as the following: (1) adsorption of CO₂ molecules on the surface in the form of double bonds, (2) activation of the adsorbed *CO₂ to obtain a carboxyl intermediate *COOH (*CO₂ + H⁺ + e⁻ → *COOH), (3) reduction and subsequent separation of *COOH through a proton-electron transfer reduction process to produce *CO (*COOH + H⁺ + e⁻ → *CO + H₂O), (4) desorption of CO (*CO → CO).

Subsequently, the adsorption and activation behaviors for CO₂ on pristine ZnIn₂S₄ and ZnIn₂S_{3.5}Se_{0.5} surfaces were theoretically investigated by first-principles density functional theory (DFT) calculations (Fig. S20). The adsorbed CO₂ (noted as *CO₂, where “*” denotes the adsorption state on the material surface) had a curved configuration with an angle of ≈ 120°, which is similar to the CO₂⁻ anion. It indicates that the activation of CO₂ molecules on both pristine ZnIn₂S₄ and ZnIn₂S_{3.5}Se_{0.5} surfaces could be achieved [57,58]. Differential charge density (DCD) and adsorption energy calculations (Fig. 6b, Table S3) display that the adsorption energy of CO₂ adsorbed by ZnIn₂S_{3.5}Se_{0.5} (-1.89 eV) is more negative than that of pristine ZnIn₂S₄ (-1.24 eV). ZnIn₂S_{3.5}Se_{0.5} has a stronger adsorption capacity for CO₂ than pristine ZnIn₂S₄. The strong binding interaction between CO₂ and ZnIn₂S_{3.5}Se_{0.5} may be due to the formed local charge polarization on the surface by Se substituting S forming, which further provide an abundance of active sites to enhance CO₂ adsorption. The free energy diagram for the adsorption and dissociation of CO₂ reduction on ZnIn₂S₄ and ZnIn₂S_{3.5}Se_{0.5} surfaces was further calculated in Fig. 6c and Fig. S21. Because of the enhanced adsorption of CO₂ on ZnIn₂S_{3.5}Se_{0.5} surface, there is a lower energy barrier to be overcome for *CO₂ adsorption on ZnIn₂S_{3.5}Se_{0.5} than that of ZnIn₂S₄. The conversion of *CO₂ to *COOH over ZnIn₂S₄ requires an energy barrier of 2.46 eV, while only 2.32 eV over ZnIn₂S_{3.5}Se_{0.5}. It indicates that the formation of *COOH on

ZnIn₂S_{3.5}Se_{0.5} surface is more favorable thermodynamically than on ZnIn₂S₄ surface. The transformation from *COOH to *CO on ZnIn₂S_{3.5}Se_{0.5} surface is easily achieved due to the downward slope of the free energy curve. Moreover, the release of CO from ZnIn₂S_{3.5}Se_{0.5} is more favorable since energy barrier for *CO desorption on ZnIn₂S_{3.5}Se_{0.5} (0.09 eV) is lower than that on ZnIn₂S₄ (0.14 eV). In brief, ZnIn₂S_{3.5}Se_{0.5} can promote CO₂ reduction due to the formed local charge polarization through Se substituting S, which could reduce the CO₂ activation energy barrier by stabilizing the *COOH intermediate.

The mechanism for improved photocatalytic performance of CO₂ reduction over ZnIn₂S_{3.5}Se_{0.5} were proposed under the effect of enhanced B-IEF based on above theoretical calculations and experimental results in Fig. 6d. The surface modification (Se atom substituting S atoms of [In-S] layers) alters the local crystal structure of the ZnIn₂S₄, which leads to surface reconstruction of electronic configuration and accelerates surface charges to accumulate in atom adjacent with Se atom. The charge polarization of [In-S] layer in turn leads to the severe inhomogeneity of charge distribution within ZnIn₂S₄, which induces an enhanced B-IEF intensity from [In-S] layer to [Zn-S] layer. It is truly that external/surface modification that affects internal regulation by modulating B-IEF intensity. Under irradiation, the photogenerated electron-hole pairs undergo effective separation under enhanced B-IEF, in which the photogenerated holes are preserved the [Zn-S] layer preferentially while the photogenerated electrons migrate to the [In-S] layer spontaneously. CO₂ molecule is more readily adsorbed on the ZnIn₂S_{3.5}Se_{0.5} surface due to charge polarization of [In-S] layer by Se atoms substituting S atoms. Finally, the adsorbed CO₂ is reduced to CO product gradually by *CO₂ → *COOH → *CO → CO process with the help of co-catalyst (Co(bpy)₃²⁺) and hole sacrificial agent (TEOA) because of the suitable CB position of ZnIn₂S_{3.5}Se_{0.5}.

4. Conclusion

In summary, nonmetallic selenium (Se) doped ZnIn₂S₄ (ZnIn₂S_{4-x}Se_x) nanosheets synthesized by simple hydrothermal method, was applied for photocatalytic CO₂ reduction. During the formation of the

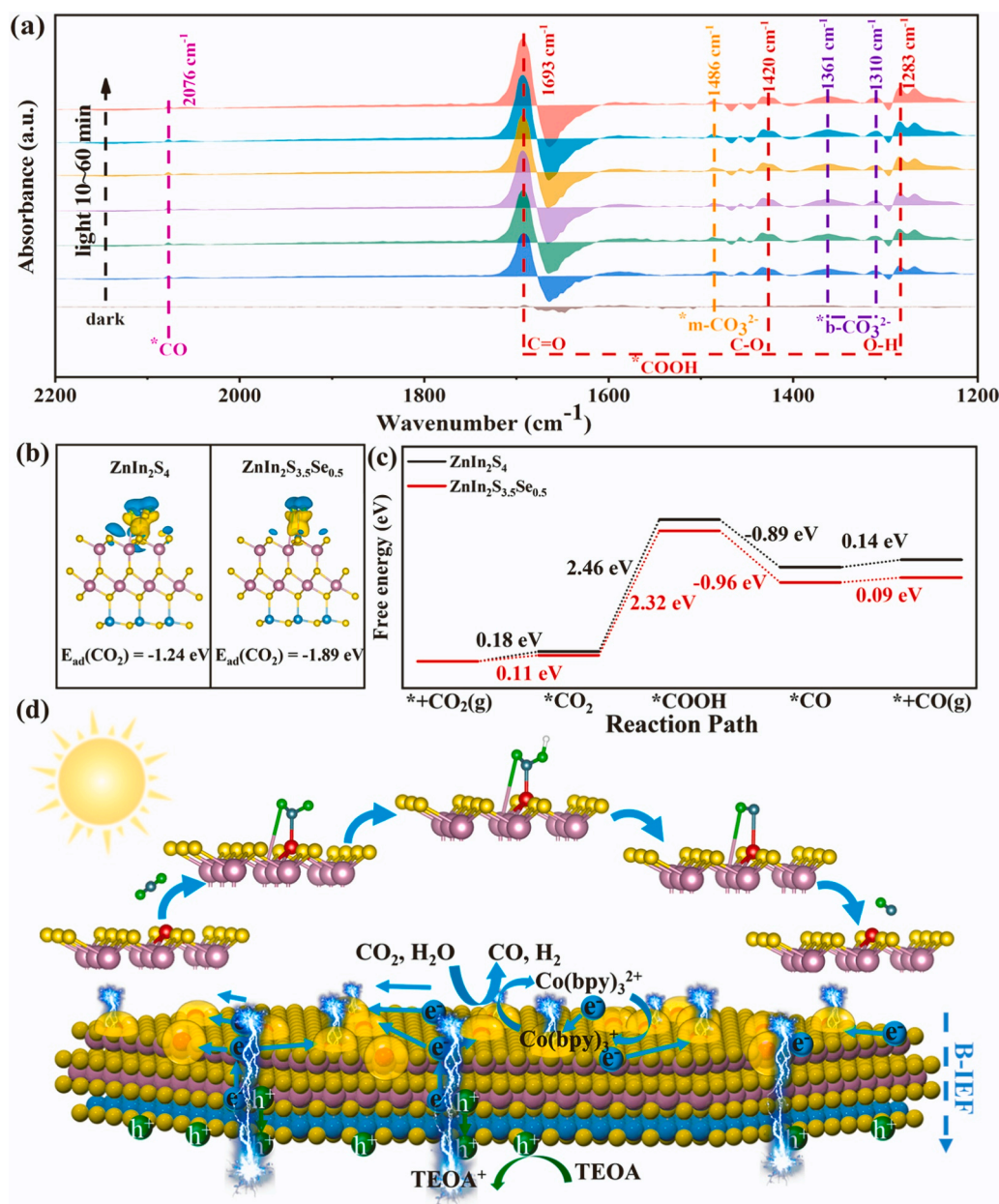


Fig. 6. (a) *In situ* FTIR spectra for adsorption and photocatalytic activation of CO₂ over ZnIn₂S_{3.5}Se_{0.5}. (b) Differential charge density and adsorption energy of CO₂ over ZnIn₂S₄ and ZnIn₂S_{3.5}Se_{0.5}. (c) Calculated free energy diagram for the adsorption and dissociation of photocatalytic CO₂ reduction on ZnIn₂S₄ and ZnIn₂S_{3.5}Se_{0.5} surfaces. (d) Schematic diagram of CO₂ adsorption, activation and conversion over ZnIn₂S₄ with Se atom substituting S atom of [In-S] layers under enhanced B-IEF.

[In-S] layer of ZnIn₂S₄, Se was doped in the tetrahedral S sites of ZnIn₂S₄, leading to a local disordered structure of the crystal and triggering a local electronic structure reconstruction, resulting in an enhanced B-IEF, which promotes the separation and transport of photogenerated charges. Simultaneously, Se doping reconfigures the active site of the reaction, enhances the adsorption capacity of the catalyst for CO₂ and lowers the activation energy barrier of CO₂, and achieves efficient and selective syngas conversion. Compared with pristine ZnIn₂S₄, the optimal Se doping amount of ZnIn₂S₄ exhibited good photocatalytic CO₂ reduction performance. The performance of ZnIn₂S_{3.5}Se_{0.5} with the best Se doping amount was 1189.5 $\mu\text{mol}\cdot\text{g}^{-1}\cdot\text{h}^{-1}$ for CO and 801.6 $\mu\text{mol}\cdot\text{g}^{-1}\cdot\text{h}^{-1}$ for H₂, with 3.87 and 1.32 times increase in CO and H₂ yields, and the CO/H₂ ratio was about 3:2. And the photocatalytic activity was maintained at 88% after 5 cycles of stability experiments. This work provides a viable strategy to overcome the slow charge kinetics and CO₂ adsorption activation difficulties of

photocatalytic CO₂ reduction and opens the way for the development of ZnIn₂S₄-based semiconductors as efficient CO₂ reduction photocatalysts.

CRediT authorship contribution statement

Xingshen Yi: Methodology, Writing – original draft, Investigation. **Shuqu Zhang:** Investigation, Writing – original draft, Writing – review & editing, Funding acquisition, Project administration. **Hao Shen:** Investigation. **Bing Li:** Supervision, Validation. **Lixia Yang:** Supervision, Validation. **Weili Dai:** Supervision, Validation. **Renjie Song:** Supervision, Validation. **Jianping Zou:** Supervision, Validation. **Shenglian Luo:** Supervision, Validation.

Declaration of Competing Interest

The authors declare that they have no known competing financial

interests or personal relationships that could have appeared to influence the work reported in this paper.

Data Availability

No data was used for the research described in the article.

Acknowledgments

This work was supported by the National Natural Science Foundation of China (52262037, 51938007) and Youth Science Foundation of Jiangxi Province (20212BAB213026). The views and ideas expressed herein are solely those of the authors and do not represent the ideas of the funding agencies in any form.

Appendix A. Supporting information

Supplementary data associated with this article can be found in the online version at [doi:10.1016/j.apcatb.2023.123003](https://doi.org/10.1016/j.apcatb.2023.123003).

References

- [1] P.M. Vitousek, H.A. Mooney, J. Lubchenco, J.M. Melillo, Human domination of Earth's ecosystems, *Science* 277 (1997) 494–499, <https://doi.org/10.1126/science.277.5325.494>.
- [2] W.H. Wang, Y. Himeda, J.T. Muckerman, G.F. Manbeck, E. Fujita, CO₂ hydrogenation to formate and methanol as an alternative to photo- and electrochemical CO₂ reduction, *Chem. Rev.* 115 (2015) 12936–12973, <https://doi.org/10.1021/acs.chemrev.5b00197>.
- [3] H. Lin, S. Luo, H. Zhang, J. Ye, Toward solar-driven carbon recycling, *Joule* 6 (2022) 294–314, <https://doi.org/10.1016/j.joule.2022.01.001>.
- [4] A. Sabbah, I. Shown, M. Qorban, F.-Y. Fu, T.-Y. Lin, H.-L. Wu, P.-W. Chung, C.-I. Wu, S.R. Merden Santiago, J.-L. Shen, K.-H. Chen, L.-C. Chen, Boosting photocatalytic CO₂ reduction in a ZnS/ZnIn₂S₄ heterostructure through strain-induced direct Z-scheme and a mechanistic study of molecular CO₂ interaction thereon, *Nano Energy* 93 (2022), 106809, <https://doi.org/10.1016/j.nanoen.2021.106809>.
- [5] G. Yang, S. Li, N. Li, P. Zhang, C. Su, L. Gong, B. Chen, C. Qu, D. Qi, T. Wang, J. Jiang, Enhanced photocatalytic CO₂ reduction through hydrophobic microenvironment and binuclear cobalt synergistic effect in metallogels, *Angew. Chem. Int. Ed.* 61 (2022), e202205585, <https://doi.org/10.1002/ange.202205585>.
- [6] F. Chen, T. Ma, T. Zhang, Y. Zhang, H. Huang, Atomic-level charge separation strategies in semiconductor-based photocatalysts, *Adv. Mater.* 33 (2021) 2005256, <https://doi.org/10.1002/adma.202005256>.
- [7] J. Luo, S. Zhang, M. Sun, L. Yang, S. Luo, J.C. Crittenden, A critical review on energy conversion and environmental remediation of photocatalysts with remodeling crystal lattice, surface, and interface, *ACS Nano* 13 (2019) 9811–9840, <https://doi.org/10.1021/acsnano.9b03649>.
- [8] L. Liu, H. Huang, Z. Chen, H. Yu, K. Wang, J. Huang, H. Yu, Y. Zhang, Synergistic polarization engineering on bulk and surface for boosting CO₂ photoreduction, *Angew. Chem. Int. Ed.* 60 (2021) 18303–18308, <https://doi.org/10.1002/ange.202106310>.
- [9] J. Yang, D. Wang, H. Han, C. Li, Roles of cocatalysts in photocatalysis and photoelectrocatalysis, *Acc. Chem. Res.* 46 (2013) 1900–1909, <https://doi.org/10.1021/ar300227e>.
- [10] H. Wang, L. Zhang, Z. Chen, J. Hu, S. Li, Z. Wang, J. Liu, X. Wang, Semiconductor heterojunction photocatalysts: design, construction, and photocatalytic performances, *Chem. Soc. Rev.* 43 (2014) 5234–5244, <https://doi.org/10.1039/c4cs00126e>.
- [11] Y.-P. Yuan, L.-W. Ruan, J. Barber, S.C.J. Loo, C. Xue, Hetero-nanostructured suspended photocatalysts for solar-to-fuel conversion, *Energy Environ. Sci.* 7 (2014) 3934–3951, <https://doi.org/10.1039/c4ee02914c>.
- [12] S. Zhang, X. Yi, G. Hu, M. Chen, H. Shen, B. Li, L. Yang, W. Dai, J. Zou, S. Luo, Configuration regulation of active sites by accurate doping inducing self-adapting defect for enhanced photocatalytic applications: a review, *Coord. Chem. Rev.* 478 (2023), 214970, <https://doi.org/10.1016/j.ccr.2022.214970>.
- [13] J. Li, L. Cai, J. Shang, Y. Yu, L. Zhang, Giant enhancement of internal electric field boosting bulk charge separation for photocatalysis, *Adv. Mater.* 28 (2016) 4059–4064, <https://doi.org/10.1002/adma.201600301>.
- [14] X. Chen, Y. Xu, X. Ma, Y. Zhu, Large dipole moment induced efficient bismuth chromate photocatalysts for wide-spectrum driven water oxidation and complete mineralization of pollutants, *Nat. Sci. Rev.* 7 (2020) 652–659, <https://doi.org/10.1093/nsr/nwz198>.
- [15] X. Yue, J. Fan, Q. Xiang, Internal electric field on steering charge migration: modulations, determinations and energy-related applications, *Adv. Funct. Mater.* 32 (2022) 2110258, <https://doi.org/10.1002/adfm.202110258>.
- [16] X. Chang, T. Wang, J. Gong, CO₂ photo-reduction: insights into CO₂ activation and reaction on surfaces of photocatalysts, *Energy Environ. Sci.* 9 (2016) 2177–2196, <https://doi.org/10.1039/c6ee00383d>.
- [17] J. Jiang, K. Zhao, X. Xiao, L. Zhang, Synthesis and facet-dependent photoreactivity of BiOCl single-crystalline nanosheets, *J. Am. Chem. Soc.* 134 (2012) 4473–4476, <https://doi.org/10.1021/ja210484t>.
- [18] Q. Luan, X. Xue, R. Li, L. Gu, W. Dong, D. Zhou, X. Wang, B. Li, G. Wang, C. Hou, Boosting photocatalytic hydrogen evolution: orbital redistribution of ultrathin ZnIn₂S₄ nanosheets via atomic defects, *Appl. Catal. B-Environ.* 305 (2022), 121007, <https://doi.org/10.1016/j.apcatb.2021.121007>.
- [19] S. Wang, Y. Wang, S.-L. Zhang, S.-Q. Zang, X.W. Lou, Supporting ultrathin ZnIn₂S₄ nanosheets on Co/N-Doped graphitic carbon nanocages for efficient photocatalytic H₂ generation, *Adv. Mater.* 31 (2019) 1903404, <https://doi.org/10.1002/adma.201903404>.
- [20] C. Du, B. Yan, G. Yang, Self-integrated effects of 2D ZnIn₂S₄ and amorphous Mo₂C nanoparticles composite for promoting solar hydrogen generation, *Nano Energy* 76 (2020), 105031, <https://doi.org/10.1016/j.nanoen.2020.105031>.
- [21] R. Yang, L. Mei, Y. Fan, Q. Zhang, R. Zhu, R. Amal, Z. Yin, Z. Zeng, ZnIn₂S₄-based photocatalysts for energy and environmental applications, *Small Methods* 5 (2021) 2100887, <https://doi.org/10.1002/smt.202100887>.
- [22] S. Zhang, Z. Zhang, Y. Si, B. Li, F. Deng, L. Yang, X. Liu, W. Dai, S. Luo, Gradient hydrogen migration modulated with self-adapting S vacancy in copper-doped ZnIn₂S₄ nanosheet for photocatalytic hydrogen evolution, *ACS Nano* 15 (2021) 15238–15248, <https://doi.org/10.1021/acsnano.1c05834>.
- [23] X. Jiao, Z. Chen, X. Li, Y. Sun, S. Gao, W. Yan, C. Wang, Q. Zhang, Y. Lin, Y. Luo, Y. Xie, Defect-mediated electron-hole separation in one-unit-cell ZnIn₂S₄ layers for boosted solar-driven CO₂ reduction, *J. Am. Chem. Soc.* 139 (2017) 7586–7594, <https://doi.org/10.1021/jacs.7b02290>.
- [24] S. Zhang, X. Liu, C. Liu, S. Luo, L. Wang, T. Cai, Y. Zeng, J. Yuan, W. Dong, Y. Pei, Y. Liu, MoS₂ quantum dot growth induced by S vacancies in a ZnIn₂S₄ monolayer: atomic-level heterostructure for photocatalytic hydrogen production, *ACS Nano* 12 (2018) 751–758, <https://doi.org/10.1021/acsnano.7b07974>.
- [25] G. Zhang, L. Yang, X. Wang, Z. Wu, J. Jiang, Y. Luo, Energy materials design for steering charge kinetics, *Adv. Mater.* 30 (2018) 1801988, <https://doi.org/10.1002/adma.201801988>.
- [26] X. Shi, C. Dai, X. Wang, J. Hu, J. Zhang, L. Zheng, L. Mao, H. Zheng, M. Zhu, Protruding Pt single-sites on hexagonal ZnIn₂S₄ to accelerate photocatalytic hydrogen evolution, *Nat. Commun.* 13 (2022) 1–10, <https://doi.org/10.1038/s41467-022-28995-1>.
- [27] J. Wan, L. Liu, Y. Wu, J. Song, J. Liu, R. Song, J. Low, X. Chen, J. Wang, F. Fu, Y. Xiong, Exploring the polarization photocatalysis of ZnIn₂S₄ material toward hydrogen evolution by integrating cascade electric fields with hole transfer vehicle, *Adv. Funct. Mater.* 32 (2022) 2203252, <https://doi.org/10.1002/adfm.202203252>.
- [28] D. Zhou, X. Xue, X. Wang, Q. Luan, A. Li, L. Zhang, B. Li, W. Dong, G. Wang, C. Hou, Ni, In co-doped ZnIn₂S₄ for efficient hydrogen evolution: modulating charge flow and balancing H adsorption/desorption, *Appl. Catal. B-Environ.* 310 (2022), 121337, <https://doi.org/10.1016/j.apcatb.2022.121337>.
- [29] W. Liu, Y. Shang, A. Zhu, P. Tan, Y. Liu, L. Qiao, D. Chu, X. Xiong, J. Pan, Enhanced performance of doped BiOCl nanoplates for photocatalysis: understanding from doping insight into improved spatial carrier separation, *J. Mater. Chem. A* 5 (2017) 12542–12549, <https://doi.org/10.1039/c7ta02724a>.
- [30] W. Xu, W. Tian, L. Meng, F. Cao, L. Li, Interfacial chemical bond-modulated Z-scheme charge transfer for efficient photoelectrochemical water splitting, *Adv. Energy Mater.* 11 (2021) 2003500, <https://doi.org/10.1002/aenm.202003500>.
- [31] C.-Q. Li, X. Du, S. Jiang, Y. Liu, Z.-L. Niu, Z.-Y. Liu, X.-Z. Yue, Constructing direct Z-scheme heterostructure by enwrapping ZnIn₂S₄ on CdS hollow cube for efficient photocatalytic H₂ generation, *Adv. Sci.* 9 (2022) 2201773, <https://doi.org/10.1002/advs.202201773>.
- [32] H.-N. Fan, X.-Y. Wang, H.-B. Yu, Q.-F. Gu, S.-L. Chen, Z. Liu, X.-H. Chen, W.-B. Luo, H.-K. Liu, Enhanced potassium ion battery by inducing interlayer anionic ligands in MoS_{1.5}Se_{0.5} nanosheets with exploration of the mechanism, *Adv. Energy Mater.* 10 (2020) 1904162, <https://doi.org/10.1002/aenm.201904162>.
- [33] Y. Huang, Z. Wang, M. Guan, F. Wu, R. Chen, Toward rapid-charging sodium-ion batteries using hybrid-phase molybdenum sulfide selenide-based anodes, *Adv. Mater.* 32 (2020) 2003534, <https://doi.org/10.1002/adma.202003534>.
- [34] C. Liu, B. Chai, C. Wang, J. Yan, Z. Ren, Solvothermal fabrication of MoS₂ anchored on ZnIn₂S₄ microspheres with boosted photocatalytic hydrogen evolution activity, *Int. J. Hydrog. Energ.* 43 (2018) 6977–6986, <https://doi.org/10.1016/j.ijhydene.2018.02.116>.
- [35] B. Pan, Y. Wu, B. Rhimi, J. Qin, Y. Huang, M. Yuan, C. Wang, Oxygen-doping of ZnIn₂S₄ nanosheets towards boosted photocatalytic CO₂ reduction, *J. Energy Chem.* 57 (2021) 1–9, <https://doi.org/10.1016/j.jechem.2020.08.024>.
- [36] P. Wang, Z. Shen, Y. Xia, H. Wang, L. Zheng, W. Xi, S. Zhan, Atomic insights for optimum and excess doping in photocatalysis: a case study of few-layer Cu-ZnIn₂S₄, *Adv. Funct. Mater.* 29 (2019) 1807013, <https://doi.org/10.1002/adfm.201807013>.
- [37] Y. Zhu, L. Wang, Y. Liu, L. Shao, X. Xia, In-situ hydrogenation engineering of ZnIn₂S₄ for promoted visible-light water splitting, *Appl. Catal. B-Environ.* 241 (2019) 483–490, <https://doi.org/10.1016/j.apcatb.2018.09.062>.
- [38] J. Qin, Q. Zhao, Y. Zhao, Y. Wu, B. Pan, C. Wang, Metal-free phosphorus-doped ZnIn₂S₄ nanosheets for enhanced photocatalytic CO₂ reduction, *J. Phys. Chem. C* 125 (2021) 23813–23820, <https://doi.org/10.1021/acs.jpcc.1c07651>.
- [39] Y. Guo, W. Shi, Y. Zhu, Y. Xu, F. Cui, Enhanced photoactivity and oxidizing ability simultaneously via internal electric field and valence band position by crystal structure of bismuth oxyiodide, *Appl. Catal. B-Environ.* 262 (2020), 118262, <https://doi.org/10.1016/j.apcatb.2019.118262>.
- [40] X. Gao, K. Gao, W. Zhu, C. Liang, Q. Li, F. Fu, Y. Zhu, Accurate guided alternating atomic layer enhance internal electric field to steering photogenerated charge

- separation for enhance photocatalytic activity, *Appl. Catal. B-Environ.* 298 (2021), 120536, <https://doi.org/10.1016/j.apcatb.2021.120536>.
- [41] X. Chen, J. Chen, Y. Chai, Z. Zhang, Y. Zhu, Efficient photocatalytic overall water splitting induced by the giant internal electric field of a g-C₃N₄/rGO/PDIP Z-scheme heterojunction, *Adv. Mater.* 33 (2021) 2007479, <https://doi.org/10.1002/adma.202007479>.
- [42] Z. Yu, K. Yang, C. Yu, K. Lu, W. Huang, L. Xu, L. Zou, S. Wang, Z. Chen, J. Hu, Y. Hou, Y. Zhu, Steering unit cell dipole and internal electric field by highly dispersed Er atoms embedded into NiO for efficient CO₂ photoreduction, *Adv. Funct. Mater.* 32 (2022) 2111999, <https://doi.org/10.1002/adfm.202111999>.
- [43] Z. Wu, J. Jing, K. Zhang, W. Li, J. Yang, J. Shen, S. Zhang, K. Xu, S. Zhang, Y. Zhu, Epitaxial BiP₅O₁₄ layer on BiOI nanosheets enhancing the photocatalytic degradation of phenol via interfacial internal-electric-field, *Appl. Catal. B-Environ.* 307 (2022), 121153, <https://doi.org/10.1016/j.apcatb.2022.121153>.
- [44] Y. Xia, Q. Li, K. Lv, D. Tang, M. Li, Superiority of graphene over carbon analogs for enhanced photocatalytic H₂-production activity of ZnIn₂S₄, *Appl. Catal. B-Environ.* 206 (2017) 344–352, <https://doi.org/10.1016/j.apcatb.2017.01.060>.
- [45] X. Jiao, Z. Chen, X. Li, Y. Sun, S. Gao, W. Yan, C. Wang, Q. Zhang, Y. Lin, Y. Luo, Y. Xie, Defect-mediated electron–hole separation in one-unit-cell ZnIn₂S₄ layers for boosted solar-driven CO₂ reduction, *J. Am. Chem. Soc.* 139 (2017) 7586–7594, <https://doi.org/10.1021/jacs.7b02290>.
- [46] W. Guo, H. Luo, Z. Jiang, D. Fang, J. Chi, W. Shangguan, Z. Wang, L. Wang, A. F. Lee, Ge-doped cobalt oxide for electrocatalytic and photocatalytic water splitting, *ACS Catal.* 12 (2022) 12000–12013, <https://doi.org/10.1021/acscatal.2c03730>.
- [47] B. Xu, Y. An, Y. Liu, X. Qin, X. Zhang, Y. Dai, Z. Wang, P. Wang, Mh. Whangboac, B. Huang, Enhancing the photocatalytic activity of BiOX (X = Cl, Br, and I), (BiO)₂CO₃ and Bi₂O₃ by modifying their surfaces with polar organic anions, 4-substituted thiophenolates, *J. Mater. Chem. A* 5 (2017) 14406–14414, <https://doi.org/10.1039/C7TA03970K>.
- [48] K. Wang, Q. Li, B. Liu, B. Cheng, W. Ho, J. Yu, Sulfur-doped g-C₃N₄ with enhanced photocatalytic CO₂-reduction performance, *Appl. Catal. B-Environ.* 176 (2015) 44–52, <https://doi.org/10.1016/j.apcatb.2015.03.045>.
- [49] M. Wang, M. Shen, X. Jin, J. Tian, M. Li, Y. Zhou, L. Zhang, Y. Li, J. Shi, Oxygen vacancy generation and stabilization in CeO_{2-x} by Cu introduction with improved CO₂ photocatalytic reduction activity, *ACS Catal.* 9 (2019) 4573–4581, <https://doi.org/10.1021/acscatal.8b03975>.
- [50] L. Wang, B. Cheng, L. Zhang, J. Yu, In situ irradiated XPS investigation on S-scheme TiO₂@ZnIn₂S₄ photocatalyst for efficient photocatalytic CO₂ reduction, *Small* 17 (2021) 2103447, <https://doi.org/10.1002/sml.202103447>.
- [51] L. Xiao, C. Yuan, P. Chen, Y. Liu, J. Sheng, S. Zhang, F. Dong, Y. Sun, Cu-S bonds as an atomic-level transfer channel to achieve photocatalytic CO₂ reduction to CO on Cu-substituted ZnIn₂S₄, *ACS Sustain. Chem. Eng.* 10 (2022) 11902–11912, <https://doi.org/10.1021/acssuschemeng.2c02919>.
- [52] X. Zhu, Y. Cao, Y. Song, J. Yang, X. She, Z. Mo, Y. She, Q. Yu, X. Zhu, J. Yuan, H. Li, H. Xu, Unique dual-sites boosting overall CO₂ photoconversion by hierarchical electron harvesters, *Small* 17 (2021) 2103796, <https://doi.org/10.1002/sml.202103796>.
- [53] N.J. Firet, W.A. Smith, Probing the reaction mechanism of CO₂ electroreduction over Ag films via operando infrared spectroscopy, *ACS Catal.* 7 (2017) 606–612, <https://doi.org/10.1021/acscatal.6b02382>.
- [54] Y. Li, S. Wang, X.-S. Wang, Y. He, Q. Wang, Y. Li, M. Li, G. Yang, J. Yi, H. Lin, D. Huang, L. Li, H. Chen, J. Ye, Facile top-down strategy for direct metal atomization and coordination achieving a high turnover number in CO₂ photoreduction, *J. Am. Chem. Soc.* 142 (2020) 19259–19267, <https://doi.org/10.1021/jacs.0c09060>.
- [55] S. Wu, Y. Ji, L. Wang, X. Wu, H. Xu, Selective CO₂-to-CH₄ photoconversion in aqueous solutions catalyzed by atomically dispersed copper sites anchored on ultrathin graphdiyne oxide nanosheets, *Sol. RRL* 5 (2021) 2100200, <https://doi.org/10.1002/solr.202100200>.
- [56] J. Sheng, Y. He, J. Li, C. Yuan, H. Huang, S. Wang, Y. Sun, Z. Wang, F. Dong, Identification of halogen-associated active sites on bismuth-based perovskite quantum dots for efficient and selective CO₂-to-CO photoreduction, *ACS Nano* 14 (2020) 13103–13114, <https://doi.org/10.1021/acsnano.0c04659>.
- [57] B. Han, X. Ou, Z. Deng, Y. Song, C. Tian, H. Deng, Y.-J. Xu, Z. Lin, Nickel metal-organic framework monolayers for photoreduction of diluted CO₂: metal-node-dependent activity and selectivity, *Angew. Chem. Int. Ed.* 57 (2018) 16811–16815, <https://doi.org/10.1002/ange.201811545>.
- [58] F. Wang, T. Hou, X. Zhao, W. Yao, R. Fang, K. Shen, Y. Li, Ordered macroporous carbonous frameworks implanted with CdS quantum dots for efficient photocatalytic CO₂ reduction, *Adv. Mater.* 33 (2021) 2102690, <https://doi.org/10.1002/adma.202102690>.